Research Square

Preprints are preliminary reports that have not undergone peer review.
They should not be considered conclusive, used to inform clinical practice,
or referenced by the media as validated information.

Symmetry Protected Bound Excitons and Spin–Orbit Coupled Optical Response in Janus GeSO Monolayers

Haiying Song

hysong@bjut.edu.cn

Beijing University of Technology

Zeeshan Abbas

Beijing University of Technology

Wenlong Zhang

Beijing University of Technology

Haozhe Wang

Beijing University of Technology

Danmin Liu

Beijing University of Technology

Shibing Liu

Beijing University of Technology

Article

Keywords:

Posted Date: November 18th, 2026

DOI: https://doi.org/10.21203/rs.3.rs-11427937/v1

License: This work is licensed under a Creative Commons Attribution 4.0 International License.
Read Full License

Additional Declarations: No competing interests reported.

Symmetry Protected Bound Excitons and Spin–Orbit Coupled Optical Response in Janus GeSO Monolayers

Zeeshan Abbas,[1,2] Haiying Song,[1,3,4,*] Wenlong Zhang,[1,3,4] Haozhe Wang,[1,3,4] Danmin Liu,[2] and Shibing Liu[1,3,4]

[1] *Strong-field and Ultrafast Photonics Lab, School of Physics and Optoelectronic Engineering, Beijing University of Technology, Beijing 100124, People's Republic of China*

[2] *Key Laboratory of Advanced Functional Material, College of Material Science and Engineering, Beijing University of Technology, Beijing 100124, People's Republic of China*

[3] *Beijing Key Laboratory of High-Energy Intelligent Pulsed Laser and Novel Applications, Beijing University of Technology, Beijing 100124, People's Republic of China*

[4] *Key Laboratory of Trans-scale Laser Manufacturing Technology, Ministry of Education, Beijing University of Technology, Beijing 100124, People's Republic of China*

(Dated: October 23, 2026)

We investigate the quasiparticle and excitonic properties of the dynamically and energetically stable Janus GeSO monolayer using a first-principles G_0W_0–Bethe–Salpeter-equation approach with two-dimensional Coulomb truncation. The relaxed monolayer is a direct-gap semiconductor with both band edges at Γ; the quasiparticle gap is 2.066 eV without spin–orbit coupling (SOC) and 2.065 eV with SOC, in contrast to the substantially underestimated PBE gaps of 0.60 and 0.56 eV, respectively. Electron–hole correlations generate a strongly bound, doubly degenerate bright exciton at 1.7468 eV without SOC, corresponding to a binding energy of 319.2 meV and an E-symmetry doublet of the C_{3v} point group. A nearby bound but optically dark state occurs at 1.997 eV and transforms as A_2, demonstrating that the bright–dark hierarchy is governed by crystal-symmetry selection rules. SOC leaves the quasiparticle gap nearly unchanged but qualitatively reorganizes the excitonic state: the bright doublet redshifts to 1.70200–1.70223 eV, its binding energy increases to approximately 363 meV, and its electron–hole amplitude is redistributed among four spinor transition channels with substantial triplet admixture. The oscillator strength of an individual lowest bright state is consequently reduced, reflecting redistribution rather than suppression of optical activity. Momentum-space analysis shows that the lowest exciton is predominantly localized around Γ, while the calculated spectra exhibit pronounced sub-gap excitonic absorption and higher-energy resonant features. These results establish Janus GeSO as a promising platform for symmetry-controlled and spinor-engineered excitonic optoelectronics and provide a general framework for distinguishing crystal-symmetry effects from SOC- and screening-induced exciton fine structure in oxide-containing Janus monolayers.

I. INTRODUCTION

The interaction between light and matter is governed fundamentally by the symmetry of the electronic states involved, which dictates which transitions are dipole-allowed, forbidden, or weak, and thereby shapes a material's absorption, emission, and optoelectronic response. Engineering these selection rules through deliberate symmetry breaking has emerged as a powerful route to control optical excitations at the nanoscale, yet a quantitative link between structural symmetry, electronic states, and optical activity remains elusive in systems where several electronic degrees of freedom coexist. Establishing this link is essential for guiding the design of energy-efficient photodetectors, light-emitting devices, and valley- and spin-based information technologies.

Two-dimensional (2D) materials provide an ideal platform for this problem, since reduced dimensionality makes both electronic structure and optical response acutely sensitive to symmetry. Since the isolation of graphene [1, 2], transition-metal dichalcogenide (TMD) monolayers MX_2 (M = Mo, W, Cr; X = S, Se, Te) have become a leading platform for low-dimensional physics [3], exhibiting an indirect-to-direct bandgap crossover upon thinning to a monolayer that enhances light–matter coupling [4–6]. Reduced dielectric screening in these systems produces tightly bound excitons with binding energies of several hundred meV [7, 8], whose accurate description requires many-body perturbation theory beyond DFT: the GW approximation yields reliable quasiparticle band structures via the dynamically screened Coulomb interaction W [9, 10], while the Bethe–Salpeter equation (BSE) built on GW-corrected states captures bound excitons and their optical activity [10, 11]. GW-BSE has thus become the benchmark method for 2D semiconductors [9–11].

Janus monolayers extend this platform by breaking the out-of-plane mirror symmetry intrinsic to symmetric MX_2 (D_{3h}), lowering the point group to C_{3v} and generating a permanent out-of-plane dipole absent in centrosymmetric compounds [12–14]. First realized experimentally in Janus MoSSe and SMoSe [12, 13], this built-in dipole simultaneously enhances mechanical [14], electronic, and optical [15] properties, redistributes electron and hole wavefunctions to produce dipolar excitons with extended lifetimes [16], and underlies applications in piezoelectricity [17], photovoltaics [18], and nanoelectronics [19], including the

* Corresponding author: hysong@bjut.edu.cn

recent observation of anomalous photovoltaic response in ∼0.67-nm-thick Janus MoSSe [18]. Because optical selection rules follow directly from point-group irreducible representations, the $D_{3h} \to C_{3v}$ reduction is expected to reorganize bright and dark excitonic states independent of spin–orbit coupling (SOC) alone.

Existing *GW*-BSE studies of Janus TMDs have quantified how the asymmetric dielectric environment modifies quasiparticle and optical gaps [15, 20, 21], revealing valley-resolved excitonic resonances at K^+/K^- [22] and, in a systematic full-spinor *GW*-BSE study of six Janus Mo/WXY monolayers, an SOC-driven splitting between A and B bright-exciton peaks of 20–40 meV that tracks the valence-band spin splitting rather than crystal symmetry alone [23]. Complementary work has resolved anisotropic Rashba spin textures as an intrinsic spinorial degree of freedom in Janus dichalcogenide and pnictide monolayers [24], while a non-local-screening theory of TMD exciton fine structure has shown that bright–dark splittings of a few tens of meV persist across dielectric environments through q-dependent Coulomb screening rather than symmetry alone [25]. In parallel, the oxychalcogenide branch of the Janus family has expanded rapidly: Janus CrXO monolayers were shown to be dynamically stable, direct-gap, strongly absorbing semiconductors driven by the large electronegativity contrast between O and a heavier chalcogen [26, 27]; atomic-scale oxidation-pathway calculations established that Janus MoSO and MoSeO form preferentially under oxygen-rich growth conditions with a well-defined diagonal oxidation pattern [28]; a Janus Al_2SO oxychalcogenide monolayer was confirmed to be dynamically and thermally stable with a tunable, defect- and doping-controllable band gap [29]; and a dedicated structural and optical study of trigonal Janus GeSO itself confirmed its direct gap, sizable built-in dipole (−0.208 Debye), and broadband visible-to-UV absorption [30]. Group-IV Janus monochalcogenides more broadly exhibit exciton binding energies of 0.20–0.37 eV from BSE calculations on Wannier-tight-binding Hamiltonians [31], and Janus ZrSSe shows binding energies near 0.53 eV with picosecond exciton lifetimes [32].

Spin–orbit coupling further enriches this landscape by lifting spin degeneracy and generating spin-valley locking, Rashba-type spin textures, and bright–dark exciton splittings that are essential for valleytronic and spintronic applications. In monolayer TMDs, SOC splits the valence band at K and K′ by ∼0.2 eV for Mo-based and ∼0.4 eV for W-based compounds, thereby defining the A and B exciton series and determining whether the lowest exciton is bright or dark [33, 34]. Recent full-spinor *GW*-BSE formulations have demonstrated that perturbative SOC captures the A–B splitting in most Janus Mo/WXY systems to within ∼10 meV, but can deviate by ∼70 meV in heavy-W compounds, emphasizing the need for nonperturbative spinorial treatments when quantitative accuracy is required [35]. Strain-tunable *GW*-BSE calculations on Janus MoSSe further showed that the A–B splitting varies by ∼24 meV under ±4% biaxial strain, directly linking lattice deformation, SOC, and optical response [36]. Theoretical reviews of SOC in 2D semiconductors have highlighted Janus monolayers as a prototypical class in which broken inversion symmetry and strong SOC jointly generate large Rashba parameters and anisotropic spin textures [37], while recent studies of Janus group-V and pnictogen-halide monolayers reported valley spin splittings up to ∼70 meV and Rashba parameters exceeding 0.7 eV Å in heavy-element systems [38, 39]. These results establish SOC as a central ingredient for interpreting exciton fine structure, dark–bright ordering, and polarization-dependent selection rules in asymmetric 2D layers.

None of these studies, however, has established whether the bright and dark excitonic states of an oxide-containing Janus monolayer follow a well-defined, symmetry-dictated hierarchy, or whether the reduced C_{3v} symmetry translates quantitatively into resolvable group-theoretical selection rules for a real material's full excitonic manifold as distinct from the SOC- and screening-driven splittings identified in [23, 25, 35, 36]. This is the central gap addressed here: a comprehensive *GW*-BSE study of the Janus GeSO monolayer, including its full bright exciton manifold, Rydberg series, binding energies, optical spectra, and real-space excitonic wavefunctions, together with a symmetry classification of the resulting bright and dark states, is absent from the literature [26, 27, 30].

In this work, we perform G_0W_0+BSE calculations to determine the quasiparticle electronic structure and excitonic properties of the Janus GeSO monolayer. Beyond the quasiparticle band structure, optical absorption spectrum, exciton binding energies, and real- and momentum-space excitonic wavefunctions, our key contribution is a symmetry analysis at the Γ point classifying the low-energy excitons by the irreducible representations of the C_{3v} point group: the lowest-energy exciton is a doubly degenerate, dipole-allowed E-symmetry state, while a nearby dark exciton transforms as the symmetry-forbidden A_2 representation. This establishes crystal symmetry, rather than SOC alone, as the governing principle for bright/dark exciton selection rules in oxide-containing Janus monolayers, providing a transferable framework for engineering excitonic optical activity in next-generation nanoscale optoelectronics.

II. THE THEORETICAL APPROACH

The electronic structure and optical excitations of the GeSO monolayer were investigated using a sequential first-principles workflow combining density-functional theory (DFT), the one-shot G_0W_0 approximation, and the Bethe–Salpeter equation (BSE). Ground-state calculations were performed with the Quantum ESPRESSO package [40, 41], whereas the quasiparticle and excitonic calculations were carried out using the YAMBO code [42]. The workflow was designed to describe the electronic gap, quasiparticle corrections, electron–hole attraction, and optical response

within a common reciprocal-space framework.

A. Ground-state calculations

The ground-state electronic structure was calculated within Kohn–Sham DFT using a plane-wave basis and optimized norm-conserving Vanderbilt pseudopotentials [43]. Structural relaxation, charge-density evaluation, and generation of the Kohn–Sham single-particle states were performed using the same pseudopotential framework. Exchange–correlation effects were described within the generalized-gradient approximation using the Perdew–Burke–Ernzerhof (PBE) functional [44]. The Kohn–Sham orbitals were expanded in plane waves up to a kinetic-energy cutoff of 70 Ry, while the Brillouin zone was sampled using a $12 \times 12 \times 1$ Monkhorst–Pack mesh [45]. The charge density and total energy were converged with respect to the plane-wave cutoff and k-point sampling before the subsequent many-body calculations were performed.

The GeSO monolayer was represented by a periodically repeated slab separated by a vacuum region of 20 Å along the out-of-plane direction. This separation minimizes the direct overlap between neighboring layers in the ground-state calculation. In the many-body calculations, the remaining electrostatic interaction between repeated images was removed explicitly by truncating the Coulomb interaction in the non-periodic direction [46, 47]. This combination of a large vacuum separation and Coulomb truncation is essential for modeling an isolated two-dimensional sheet rather than an artificial three-dimensional stack.

B. Quasiparticle electronic structure

The Kohn–Sham eigenvalues and wave functions obtained from the converged DFT calculation were used as the starting point for the one-shot G_0W_0 calculation [48–50]. The Brillouin zone was sampled on a $26 \times 26 \times 1$ grid for the quasiparticle calculation. The dielectric response was represented in a plane-wave basis with a reciprocal-space response cutoff of 12 Ry, while a 60 Ry plane-wave cutoff was used for the Fourier representation of the response functions and related matrix elements. A broad set of occupied and empty states was included in the polarizability and self-energy calculations to reduce the dependence of the quasiparticle energies on the unoccupied-state manifold. The high-energy contribution of the empty states was treated using an analytic terminator procedure [51].

For the low-energy quasiparticle electronic structure, the active band manifold consisted of the four highest valence bands and the four lowest conduction bands. These bands were retained in the quasiparticle analysis because they define the near-gap electronic transitions relevant to the optical response. The dielectric screening and self-energy construction included additional states outside this active manifold to ensure convergence of the screened interaction and correlation self-energy. Thus, the band window used to analyze the low-energy quasiparticle structure was distinguished from the larger intermediate-state space required to construct the many-body quantities.

The quasiparticle energies were obtained from the perturbative solution of the Dyson equation,

$$E^{\mathrm{QP}}_{n\mathbf{k}} = \varepsilon^{\mathrm{DFT}}_{n\mathbf{k}} + Z_{n\mathbf{k}}\,\mathrm{Re}\left\langle n\mathbf{k}\left|\Sigma(\varepsilon^{\mathrm{DFT}}_{n\mathbf{k}}) - V_{\mathrm{xc}}\right|n\mathbf{k}\right\rangle, \quad (1)$$

where $\varepsilon^{\mathrm{DFT}}_{n\mathbf{k}}$ is the Kohn–Sham eigenvalue, V_{xc} is the PBE exchange–correlation potential, and Σ is the GW self-energy. The renormalization factor is defined as

$$Z_{n\mathbf{k}} = \left[1 - \left.\frac{\partial\,\mathrm{Re}\,\Sigma_{n\mathbf{k}}(\omega)}{\partial\omega}\right|_{\omega=\varepsilon^{\mathrm{DFT}}_{n\mathbf{k}}}\right]^{-1}. \quad (2)$$

The self-energy is decomposed into exchange and correlation parts,

$$\Sigma(\mathbf{r},\mathbf{r}';\omega) = \Sigma_x(\mathbf{r},\mathbf{r}') + \Sigma_c(\mathbf{r},\mathbf{r}';\omega), \quad (3)$$

where

$$\Sigma_c(\mathbf{r},\mathbf{r}';\omega) = \frac{i}{2\pi}\int d\omega'\, G_0(\mathbf{r},\mathbf{r}';\omega+\omega')W_0(\mathbf{r},\mathbf{r}';\omega')e^{i\eta\omega'}. \quad (4)$$

The frequency dependence of the screened interaction was represented using a plasmon-pole model [49]. The resulting quasiparticle energies were used to determine the many-body band gap and to construct the independent-particle transition energies entering the BSE Hamiltonian.

C. Dielectric screening and two-dimensional electrostatics

The dielectric screening was calculated within the random-phase approximation. The independent-particle polarizability was evaluated as

$$\chi^0_{\mathbf{G}\mathbf{G}'}(\mathbf{q},\omega) = \frac{1}{\Omega}\sum_{nm\mathbf{k}}\frac{f_{n\mathbf{k}} - f_{m,\mathbf{k}+\mathbf{q}}}{\omega - (\varepsilon_{m,\mathbf{k}+\mathbf{q}} - \varepsilon_{n\mathbf{k}}) + i\eta} \times \rho^{\mathbf{G}}_{nm}(\mathbf{k},\mathbf{q})\left[\rho^{\mathbf{G}'}_{nm}(\mathbf{k},\mathbf{q})\right]^*, \quad (5)$$

where $f_{n\mathbf{k}}$ is the occupation factor and

$$\rho^{\mathbf{G}}_{nm}(\mathbf{k},\mathbf{q}) = \left\langle n\mathbf{k}\left|e^{-i(\mathbf{q}+\mathbf{G})\cdot\mathbf{r}}\right|m,\mathbf{k}+\mathbf{q}\right\rangle. \quad (6)$$

The inverse dielectric matrix is obtained from

$$\varepsilon^{-1}_{\mathbf{G}\mathbf{G}'}(\mathbf{q},\omega) = \left[\delta_{\mathbf{G}\mathbf{G}'} - v(\mathbf{q}+\mathbf{G})\chi^0_{\mathbf{G}\mathbf{G}'}(\mathbf{q},\omega)\right]^{-1}, \quad (7)$$

and the screened Coulomb interaction is

$$W_{\mathbf{G}\mathbf{G}'}(\mathbf{q},\omega) = \varepsilon^{-1}_{\mathbf{G}\mathbf{G}'}(\mathbf{q},\omega)v(\mathbf{q}+\mathbf{G}'). \quad (8)$$

The non-periodic electrostatics of the monolayer was treated using a slab-truncated Coulomb interaction [46].

In reciprocal space, the truncated interaction can be written generally as

$$v^{2D}(\mathbf{q}_\parallel, G_z) = \frac{4\pi}{|\mathbf{q}_\parallel|^2 + G_z^2} F_{\mathrm{slab}}(\mathbf{q}_\parallel, G_z; L_z), \tag{9}$$

where F_{slab} removes the interaction between periodic images along the out-of-plane direction. The same electrostatic treatment was retained in the dielectric, quasiparticle, and excitonic calculations. The small-q contribution was evaluated using random integration of the Coulomb singularity, which is required to describe the long-wavelength response of an isolated 2D layer [42]. In the long-wavelength limit, the resulting screening is qualitatively different from the bulk three-dimensional form and is connected with the nonlocal 2D dielectric response discussed by Cudazzo *et al.* [52, 53].

D. Bethe–Salpeter equation

The BSE calculations were performed on a dense $54 \times 54 \times 1$ Brillouin-zone grid in order to resolve the strongly varying electron–hole interaction near the optical limit. The same active band manifold used for the low-energy quasiparticle analysis was employed in the BSE: four highest valence bands and four lowest conduction bands. Accordingly, the excitonic basis contains all transitions formed from these eight bands over the complete BSE k-point grid. Additional bands were not included in the electron–hole Hamiltonian because the targeted spectrum concerns the low-energy optical response; the larger intermediate-state manifold used to construct the dielectric screening remains distinct from the BSE transition basis.

The correlated excitonic states were expanded in the basis of valence-to-conduction transitions,

$$|\lambda\rangle = \sum_{vc\mathbf{k}} A^{\lambda}_{vc\mathbf{k}} |v\mathbf{k}\, c\mathbf{k}\rangle, \tag{10}$$

where $A^{\lambda}_{vc\mathbf{k}}$ are the exciton amplitudes. The BSE eigenvalue problem is

$$\sum_{v'c'\mathbf{k}'} H^{\mathrm{BSE}}_{vc\mathbf{k},v'c'\mathbf{k}'} A^{\lambda}_{v'c'\mathbf{k}'} = E_\lambda A^{\lambda}_{vc\mathbf{k}}, \tag{11}$$

with

$$H^{\mathrm{BSE}}_{vc\mathbf{k},v'c'\mathbf{k}'} = \left(E^{\mathrm{QP}}_{c\mathbf{k}} - E^{\mathrm{QP}}_{v\mathbf{k}}\right)\delta_{vv'}\delta_{cc'}\delta_{\mathbf{k}\mathbf{k}'} + K_{vc\mathbf{k},v'c'\mathbf{k}'}. \tag{12}$$

The electron–hole interaction kernel was constructed from the attractive statically screened direct term and the repulsive bare exchange term [50, 54, 55],

$$K = K^x - K^d. \tag{13}$$

The direct contribution is

$$K^d_{vc\mathbf{k},v'c'\mathbf{k}'} = \sum_{\mathbf{G}\mathbf{G}'} M^{\mathbf{G}}_{vv'}(\mathbf{k},\mathbf{k}') W_{\mathbf{G}\mathbf{G}'}(\mathbf{k}-\mathbf{k}', 0) \left[M^{\mathbf{G}'}_{cc'}(\mathbf{k},\mathbf{k}')\right]^*, \tag{14}$$

where

$$M^{\mathbf{G}}_{nn'}(\mathbf{k},\mathbf{k}') = \left\langle n\mathbf{k} \left| e^{i(\mathbf{k}'-\mathbf{k}+\mathbf{G})\cdot\mathbf{r}} \right| n'\mathbf{k}' \right\rangle. \tag{15}$$

The exchange contribution is

$$K^x_{vc\mathbf{k},v'c'\mathbf{k}'} = \sum_{\mathbf{G}\neq 0} M^{\mathbf{G}}_{vc}(\mathbf{k},\mathbf{k}) v(\mathbf{G}) \left[M^{\mathbf{G}}_{v'c'}(\mathbf{k}',\mathbf{k}')\right]^*. \tag{16}$$

The transition space was restricted to the four highest valence and four lowest conduction bands, while the optical limit corresponds to vanishing transferred photon momentum. The resonant electron–hole sector was constructed first, followed by the causal BSE solution. The resulting excitonic states provide both the excitation energies and the momentum-dependent electron–hole amplitudes.

E. Optical response and exciton properties

The coupling of an exciton to linearly polarized light is described by

$$D_\lambda(\hat{\mathbf{e}}) = \sum_{vc\mathbf{k}} A^{\lambda}_{vc\mathbf{k}} \langle v\mathbf{k} | \hat{\mathbf{e}}\cdot\mathbf{r} | c\mathbf{k}\rangle. \tag{17}$$

The corresponding momentum-resolved oscillator strength is

$$I_\lambda(\mathbf{k};\hat{\mathbf{e}}) = \left| \sum_{vc} A^{\lambda}_{vc\mathbf{k}} \langle v\mathbf{k} | \hat{\mathbf{e}}\cdot\mathbf{r} | c\mathbf{k}\rangle \right|^2. \tag{18}$$

This quantity identifies the regions of the Brillouin zone that contribute to a particular exciton and allows possible polarization-dependent or anisotropic excitonic behavior to be analyzed [56].

For an isolated 2D sheet, the optical response is expressed through the sheet polarizability rather than the dielectric function of the entire supercell [52, 53],

$$\alpha_{2D}(\omega) = -\frac{2}{A}\sum_\lambda \frac{|D_\lambda|^2}{\omega - E_\lambda + i\eta}, \tag{19}$$

where A is the in-plane unit-cell area and η is the spectral broadening. The absorption spectrum is proportional to $\mathrm{Im}\,\alpha_{2D}(\omega)$. The exciton binding energy is defined as

$$E_b = E^{\mathrm{QP}}_g - E^{\mathrm{opt}}_\lambda, \tag{20}$$

where E^{QP}_g is the quasiparticle gap and E^{opt}_λ is the energy of the selected optical exciton.

The excitonic eigenvectors were also analyzed in real space. For a fixed hole position $\mathbf{r}_h$, the electron–hole amplitude is

$$\Psi_\lambda(\mathbf{r}_e,\mathbf{r}_h) = \sum_{vc\mathbf{k}} A^{\lambda}_{vc\mathbf{k}} \psi_{c\mathbf{k}}(\mathbf{r}_e)\psi^*_{v\mathbf{k}}(\mathbf{r}_h), \tag{21}$$

which provides information about the spatial extent, localization, and anisotropy of the electron–hole pair.

F. Summary of numerical setup

The ground-state calculation used a 70 Ry plane-wave cutoff, a $12 \times 12 \times 1$ Monkhorst–Pack mesh, and a 20 Å vacuum spacing. The quasiparticle calculation employed a denser $26 \times 26 \times 1$ mesh for Brillouin-zone integration, a 12 Ry dielectric-response cutoff, and a 60 Ry plane-wave representation of the response functions. The BSE calculation used a $54 \times 54 \times 1$ mesh and included the four highest valence bands and four lowest conduction bands. The same eight-band active manifold was used in the low-energy GW band analysis and in the BSE Hamiltonian, whereas additional intermediate states were retained only in the construction of the dielectric matrix and self-energy. Coulomb truncation, small-q integration, and reciprocal-space convergence were applied consistently across the screening, quasiparticle, and excitonic stages. This protocol follows established GW–BSE practice for low-dimensional semiconductors [42, 50, 56].

III. RESULTS AND DISCUSSION

The optimized 1T Janus GeSO monolayer crystallizes in the trigonal $P3m1$ space group, preserving the hexagonal in-plane framework while breaking the out-of-plane mirror symmetry due to the different chalcogen species on the two sides of the Ge layer. The calculated lattice constant is $a = 3.19$ Å, with a vacuum spacing of 20 Å introduced along the out-of-plane direction to avoid spurious interlayer interactions between periodic images. The Fig. 1 relaxed fractional coordinates show that the Ge atom is located near the central plane, whereas the S and O atoms occupy opposite sides of it, confirming the intrinsic Janus asymmetry of the monolayer. The dynamical stability of monolayer GeSO was investigated using density-functional perturbation theory (DFPT). The calculated phonon dispersion along the high-symmetry directions of the Brillouin zone is shown in Fig. 2. No imaginary phonon frequencies are observed throughout the Brillouin zone, confirming the dynamical stability of the GeSO monolayer.

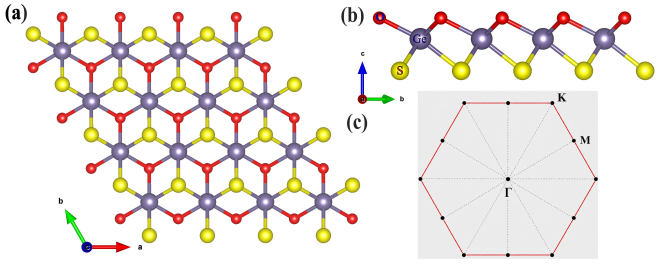


FIG. 1. Optimized crystal structure and Brillouin zone of the Janus GeSO monolayer: (a) top view, (b) side view, and (c) first Brillouin zone showing the high-symmetry points used for the electronic structure calculations.

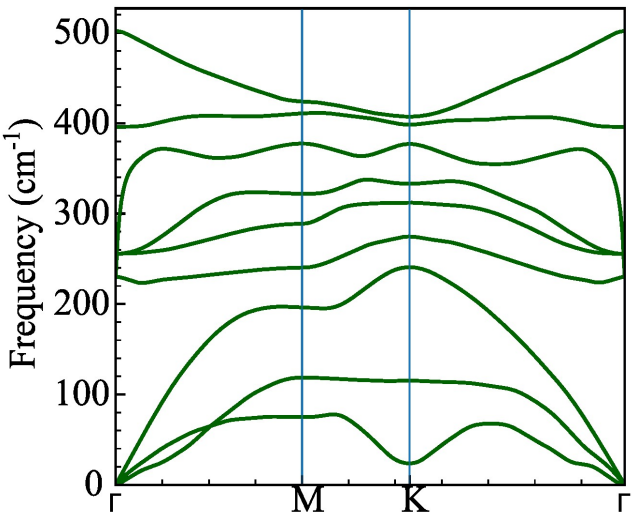


FIG. 2. Phonon dispersion of monolayer GeSO calculated using density-functional perturbation theory along the high-symmetry directions of the Brillouin zone. The absence of imaginary frequencies confirms the dynamical stability of the structure.

We further assessed the energetic stability of GeSO by calculating its formation energy and constructing the convex hull of the ternary Ge–S–O chemical space. The formation energy per atom is defined as

$$\Delta E_{\mathrm{f}} = \frac{E_{\mathrm{GeSO}} - (\mu_{\mathrm{Ge}} + \mu_{\mathrm{S}} + \mu_{\mathrm{O}})}{3}, \tag{22}$$

where E_{GeSO} is the total energy of GeSO per formula unit and μ_i denotes the energy per atom of the corresponding elemental reference state. The calculated formation energy is $\Delta E_{\mathrm{f}} = -2.121132$ eV/atom, indicating favorable formation relative to the elemental constituents.

The convex-hull construction in Fig. 3 identifies the lowest-energy decomposition pathway as

$$\mathrm{GeSO} \rightarrow \frac{1}{2}\mathrm{GeS_2} + \frac{1}{2}\mathrm{GeO_2}. \tag{23}$$

GeSO lies 0.711132 eV/atom below the corresponding GeS_2–GeO_2 tie line, demonstrating energetic stability against this decomposition pathway. Together with the absence of imaginary phonon modes, these results establish the dynamical and thermodynamic stability of monolayer GeSO.

A. Electronic Properties

The electronic band structures of the Janus GeSO monolayer obtained within the DFT and G_0W_0 frameworks are presented in Fig. 2 along the high-symmetry path Γ–M–K–Γ. Panels (a) and (b) show the results without spin–orbit coupling (SOC), while panels (c) and (d) include SOC. In

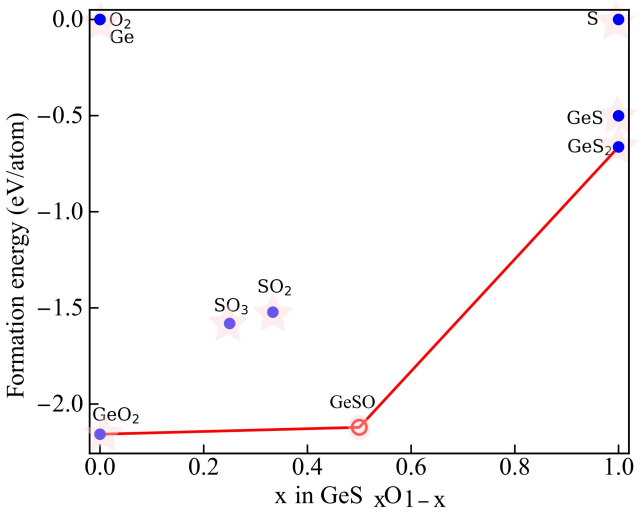


FIG. 3. Formation-energy convex hull of the ternary Ge–S–O chemical space. GeSO lies 0.711132 eV/atom below the GeS_2–GeO_2 tie line, indicating energetic stability against decomposition into these competing phases.

all cases, GeSO retains a direct-band-gap character, with both the valence-band maximum (VBM) and conduction-band minimum (CBM) located at the Γ point. This finding is consistent with previous theoretical reports, which predicted GeSO to be a direct-gap semiconductor with PBE and HSE06 band gaps of 0.63 and 1.55 eV, respectively [57]. In the present work, DFT calculations yield a band gap of 0.60 eV in the absence of spin–orbit coupling (SOC). Including quasiparticle corrections within the G_0W_0 approximation substantially increases the band gap to 2.066 eV. When SOC is included, the DFT band gap decreases slightly to 0.56 eV, whereas the G_0W_0 gap remains nearly unchanged at 2.065 eV, indicating that SOC has only a minor effect on the overall band-gap renormalization. These results are shown in Fig. 4(a) and Fig. 4(b) for calculations without and with SOC, respectively. Table I summarizes the calculated band gaps alongside previously reported theoretical values, demonstrating the agreement of the present DFT results with the literature and the substantial quasiparticle corrections introduced by the G_0W_0 approximation.

TABLE I. Calculated band gaps of the Janus GeSO monolayer compared with previous theoretical results. All values are in eV.

Method	SOC	E_g (eV)	Character	Reference
PBE (this work)	no	0.60	Direct (Γ–Γ)	–
PBE	no	0.63	Direct (Γ–Γ)	[57]
HSE06	no	1.55	Direct (Γ–Γ)	[57]
PBE (this work)	yes	0.56	Direct (Γ–Γ)	–
G_0W_0 (this work)	no	2.066	Direct (Γ–Γ)	–
G_0W_0 (this work)	yes	2.065	Direct (Γ–Γ)	–

The pronounced enhancement of the band gap reflects the importance of many-body interactions in accurately describing the electronic structure of two-dimensional materials. In reduced dimensions, the weakened dielectric screening amplifies electron–electron interactions, leading to self-energy corrections that are not adequately captured within conventional semilocal exchange–correlation functionals. Consequently, the quasiparticle spectrum exhibits a considerably larger energy separation between the occupied and unoccupied states than that predicted by DFT. The substantial difference between the DFT and G_0W_0 band gaps therefore underscores the critical role of quasiparticle corrections in obtaining an accurate description of the electronic properties of the GeSO monolayer and establishes the G_0W_0 electronic structure as the appropriate foundation for the subsequent excitonic and optical investigations.

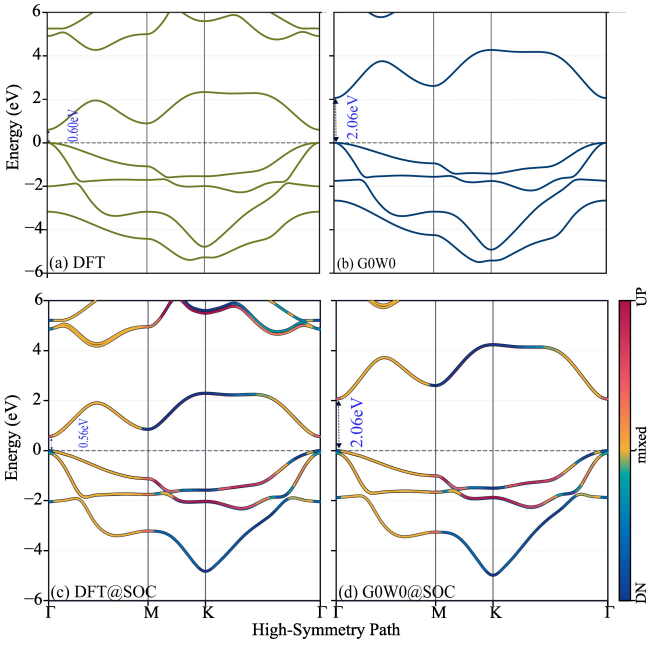


FIG. 4. Electronic band structures of the GeSO monolayer along the high-symmetry path $\Gamma \to M \to K \to \Gamma$, obtained using DFT (a,c) and G_0W_0 (b,d) approaches. Panels (a) and (b) are without SOC, while panels (c) and (d) include SOC. The arrows indicate the direct band gap in each case.

Figure 5(a) presents the *GW* orbital-projected band structure of the Janus GeSO monolayer, providing a momentum-resolved picture of the atomic-orbital contributions to the quasiparticle electronic states. The electronic states in the vicinity of the fundamental band gap are predominantly derived from the chalcogen p orbitals, indicating that the low-energy electronic structure is governed primarily by the S and O sublattices. The highest valence band exhibits a pronounced S-3p character around the Γ and K high-symmetry points, while the O-2p contribution becomes increasingly significant along the Γ–M direction, giving rise to strong S–O orbital hybridization within the upper valence manifold. Likewise,

the lowest conduction band is characterized by a nearly uniform hybridization of S-3p and O-2p orbitals throughout the Brillouin zone, accompanied by only a weak Ge-4s contribution. The negligible participation of Ge orbitals at the band edges indicates that the fundamental electronic transitions are predominantly associated with the chalcogen-derived electronic states.

The orbital-resolved nature of the band structure is further substantiated by the GW projected density of states (PDOS) shown in Fig. 5(b), which provides the corresponding energy-resolved distribution of the electronic states. The valence-band manifold is dominated by overlapping O-2p and S-3p states, reflecting the strong hybridization observed in the band structure. The largest spectral weight originates from the O-2p orbitals approximately 2 eV below the valence-band maximum, whereas a pronounced secondary peak associated with S-3p states appears around 3.5 eV below the band edge. In contrast, the lowest conduction states arise from weak hybridization among Ge-4s, S-3p, and O-2p orbitals, forming an isolated conduction manifold extending over approximately 5 eV. Beyond this energy range, the electronic structure becomes increasingly dominated by Ge-4p states, which constitute the principal contribution to the higher-lying conduction bands. The excellent agreement between the k-resolved orbital projections and the energy-resolved PDOS establishes a consistent microscopic picture in which the quasiparticle states near the fundamental band gap are governed by hybridized chalcogen p orbitals, while the Ge orbitals become electronically significant only at higher excitation energies.

IV. NOMENCLATURE

To distinguish the relevant low- and high-energy BSE eigenstates of monolayer GeSO, we use the following nomenclature. The state $\boldsymbol{\beta_0}$ denotes the lowest-energy dark bound exciton, located at approximately 1.997 eV in the no-SOC calculation and characterized by an almost vanishing oscillator strength. The symbols $\boldsymbol{\beta_1}$ and $\boldsymbol{\beta_2}$ denote the two degenerate partners of the lowest bright bound-exciton doublet in the scalar-relativistic calculation. Both occur at 1.7468 eV. When SOC is included, the corresponding SOC-renormalized doublet is denoted by $\boldsymbol{\beta_1^{SOC}}$ and $\boldsymbol{\beta_2^{SOC}}$, with excitation energies of 1.70200 and 1.70223 eV, respectively. Finally, $\boldsymbol{\beta_3}$–$\boldsymbol{\beta_5}$ denote higher-energy resonant excitonic features embedded in the interband continuum.

This notation distinguishes true sub-gap bound excitons (β_0, β_1, and β_2) from the higher-energy resonant continuum features (β_3–β_5). The latter are optically active owing to electron–hole interaction effects, but they are not discrete bound electron–hole pairs and therefore do not possess a positive discrete exciton binding energy.

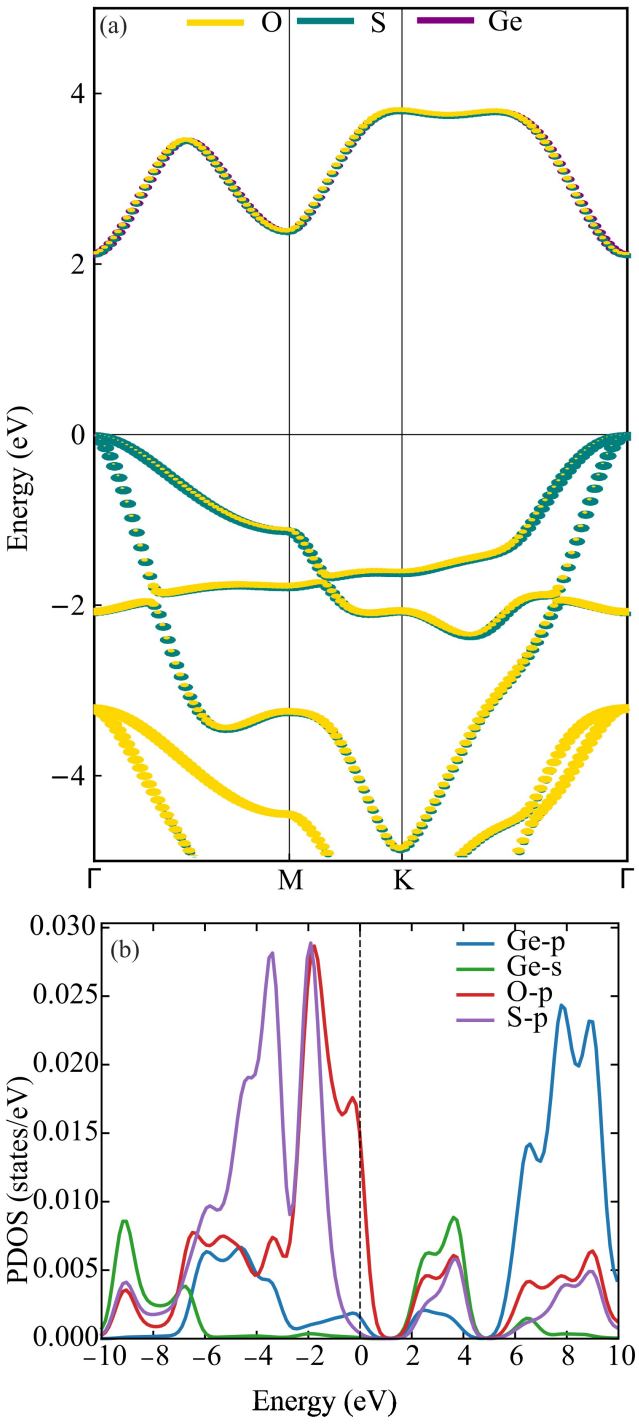


FIG. 5. (a) GW orbital-projected band structure of the Janus GeSO monolayer along the high-symmetry path $\Gamma \to M \to K \to \Gamma$, illustrating the orbital contributions of Ge-4s, Ge-4p, S-3p, and O-2p states to the quasiparticle bands. The size of the colored markers is proportional to the corresponding orbital weight. (b) GW projected density of states (PDOS) resolved into Ge-4s, Ge-4p, S-3p, and O-2p orbitals. The Fermi level is set to 0 eV in both panels.

A. Optical Absorption Spectrum and the E-Derived Exciton Manifold

The optical absorption spectrum of the Janus GeSO monolayer, calculated in the $q \to 0$ limit from the macroscopic dielectric function, is shown in Figs. 6(a) and 6(b). The spectra are evaluated for in-plane light polarization $(1, 1, 0)$ within the independent-particle approximation (IPA), the independent-particle approximation based on GW quasiparticle energies (GW-IPA), and the GW+BSE formalism. While the IPA and GW-IPA spectra describe single-particle interband transitions, the inclusion of electron–hole interactions within the BSE produces pronounced excitonic resonances that dominate the low-energy optical response. The converged GW calculations yield direct quasiparticle band gaps of $E_g^{GW,\mathrm{noSOC}} = 2.066$ eV, and $E_g^{GW,\mathrm{SOC}} = 2.065$ eV. Thus, SOC changes the fundamental quasiparticle gap by only 1 meV. Consequently, the major SOC effect in GeSO is not a significant single-particle gap renormalization, but rather a modification of the electron–hole correlation, spinor composition, and optical transition strength of the excitons.

Without SOC, the GW+BSE spectrum is dominated by the bright bound-exciton doublet β_1, β_2, whose two components occur at 1.7468 eV. Their binding energy is obtained from $E_b = E_g^{GW} - E_X$ and is therefore $E_b^{\mathrm{noSOC}}(\beta_1, \beta_2) = 0.3192$ eV. The binding energy of 319.2 meV is substantial and reflects reduced dielectric screening and enhanced electron–hole attraction in the two-dimensional Janus GeSO monolayer. The two states β_1 and β_2 are the partners of the two-dimensional E irreducible representation of the C_{3v} point group. Their degeneracy is therefore a consequence of crystal symmetry, rather than spin–orbit coupling.

With SOC, the lowest strongly bright doublet is redshifted to 1.70200 and 1.70223 eV, denoted by β_1^{SOC} and β_2^{SOC}, respectively. Using the SOC quasiparticle gap, the binding energy of the lowest bright SOC exciton is $E_b^{\mathrm{SOC}}(\beta_1^{\mathrm{SOC}}) = 0.3630$ eV.therefore redshifts the lowest strongly bright exciton by approximately 44.8 meV and increases its binding energy by approximately 43.8 meV relative to the no-SOC result, while the quasiparticle gap remains nearly unchanged.

A dark excitonic state, β_0, is identified at approximately 1.997 eV in the no-SOC calculation, exhibiting an almost vanishing oscillator strength. It remains a bound exciton with respect to the no-SOC GW gap, with $E_b(\beta_0) \approx 0.069$ eV. The dark state lies approximately 250 meV above the bright β_1, β_2 doublet. Although it is not visible in linear optical absorption, it can influence exciton relaxation and thermal population dynamics.

Between the discrete bound-exciton manifold and the high-energy absorption region, the spectrum contains a dense set of weakly absorbing states associated with the discretized two-dimensional electron–hole continuum. Additional intense features, labeled β_3–β_5, occur at energies above the GW quasiparticle gap. These features are resonant excitons rather than discrete bound excitons: electron–hole interactions reshape the interband continuum and transfer oscillator strength into pronounced optical resonances, but these states lie within the continuum of electronic transitions and do not possess a positive discrete binding energy.

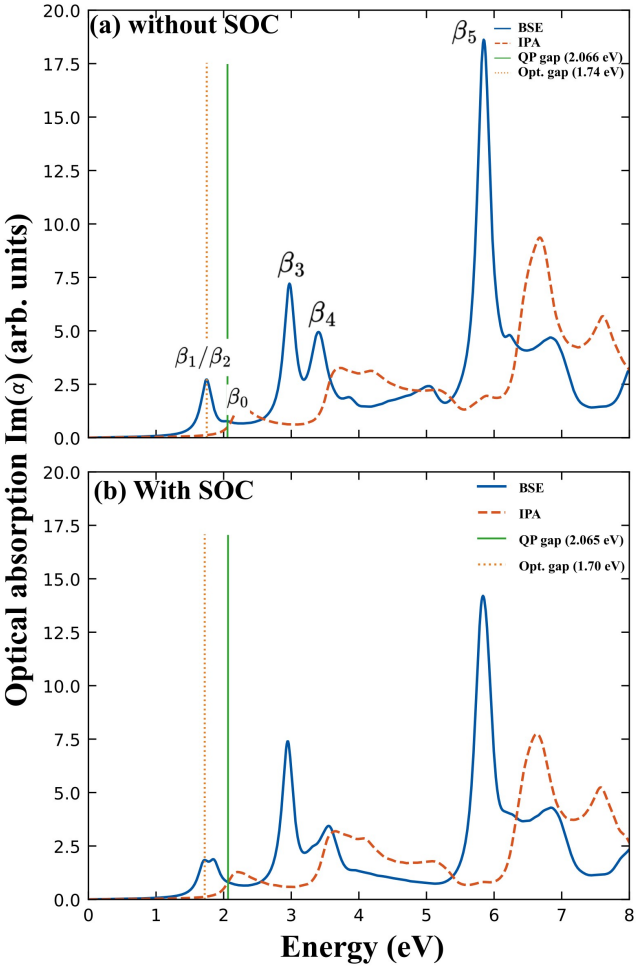


FIG. 6. Optical absorption spectra of the Janus GeSO monolayer for in-plane polarized light along $(1, 1, 0)$, obtained within the independent-particle approximation (IPA) and the GW+BSE approach: (a) without SOC and (b) with SOC. The electron–hole interaction captured by the BSE formalism produces pronounced excitonic resonances and significantly reshapes the low-energy optical response.

B. β_1, β_2: Ground Bound Exciton Doublet Without SOC

Without SOC, the lowest bright bound exciton doublet occurs at $E(\beta_1) = E(\beta_2) = 1.7468$ eV, with a binding energy of $E_b(\beta_1, \beta_2) = 319.2$ meV and oscillator strengths of $S = 0.683$ (β_1) and $S = 0.629$ (β_2). The two components are split by only 0.04 meV, consistent with exact degeneracy enforced by crystal symmetry. The combined

oscillator strength of the doublet, $S \approx 1.31$, makes it the dominant sub-gap optical transition in the scalar-relativistic description.

Microscopically, the doublet is a two-channel electron–hole superposition. For clarity and to avoid dependence on numerical band indices, the relevant states are denoted by the valence-band maximum (VB), the next lower valence band (VB−1), the conduction-band minimum (CB), and the next higher conduction band (CB+1). Without SOC, the exciton is composed of VB→CB and VB−1 →CB transitions with weights of 0.7804 (66.4%) and 0.3949 (33.6%), respectively. The direct band-edge VB→CB transition consequently dominates, while the VB−1 →CB channel provides a substantial orbital-mixing contribution.

The internal splitting between VB and VB−1 is negligible at Γ ($\Delta E \approx 0.01$ meV) but grows away from the zone center, reaching 20.9 meV at the k_2 shell, 60.6 meV at the k_{38} shell, and 80.5 meV at the k_3 shell. Since this structure exists in the calculation without SOC, it is orbital in origin and reflects crystal-field/hybridization effects rather than spin splitting. The BSE amplitude is distributed over several k-shells, consistent with a moderately delocalized two-dimensional Wannier-like exciton.

C. SOC-Renormalized Bright Doublet

Upon inclusion of SOC, the same E-derived bright doublet remains nearly degenerate and is denoted β_1^{SOC} and β_2^{SOC}. The SOC calculation yields $E(\beta_1^{\mathrm{SOC}}) = 1.70200$ eV and $E(\beta_2^{\mathrm{SOC}}) = 1.70223$ eV, separated by only 0.23 meV, with a binding energy of $E_b(\beta_1^{\mathrm{SOC}}) = 363.0$ meV. The lowest strongly bright SOC state has an oscillator strength of $S = 0.201$, while its nearly degenerate partner has $S = 0.175$. Spin-resolved BSE analysis gives approximately 24.7% singlet weight (W_S) and 75.3% triplet weight (W_T), demonstrating substantial SOC-induced spin mixing.

The SOC bright exciton is no longer described by only two electron–hole channels. Instead, it is a coherent four-channel superposition of VB→CB, VB−1 →CB, VB→CB+1, and VB−1 →CB+1 transitions, with corresponding BSE weights of 0.8023 (30.5%), 0.6461 (24.5%), 0.6212 (23.6%), and 0.5625 (21.4%), respectively. The nearly uniform distribution among the four components demonstrates that SOC redistributes the electron–hole amplitude across the spinor band-edge manifold instead of leaving the optical transition strength concentrated in one direct transition.

At Γ, the SOC partner states are degenerate. Away from Γ, SOC lifts the degeneracy asymmetrically: the splitting between CB and CB+1 reaches 14.1 meV at k_2, 20.9 meV at k_{29}, and 22.7 meV at k_3, whereas the splitting between VB and VB−1 is much smaller, namely 1.6, 3.8, and 3.0 meV at the corresponding shells. Hence, the conduction-band edge is considerably more SOC-sensitive than the valence-band edge.

Fig 7 summarizes the microscopic reorganization of the lowest bright exciton upon including SOC. In the scalar-relativistic description Fig. 7(a), the electron–hole envelope is dominated by the direct VB→CB transition, with a smaller but non-negligible VB−1 →CB contribution. SOC activates the CB+1 partner and converts this two-channel state into a four-channel spinor exciton Fig. 7(b). Consequently, no individual transition dominates the SOC exciton; rather, the physical optical excitation is a coherent superposition of all four band-edge channels. This channel proliferation provides a microscopic explanation for the strong reduction of the oscillator strength of the individual lowest bright SOC state relative to the no-SOC state.

Fig 7(c) further separates the two sources of near-edge fine structure. The larger VB–VB−1 splitting in the no-SOC calculation is orbital in origin, whereas the SOC calculation produces a smaller VB–VB−1 splitting and a more appreciable CB–CB+1 splitting. SOC therefore primarily redistributes optical amplitude through spinor mixing and activates additional electron–hole pathways, while the substantial no-SOC valence fine structure arises from orbital hybridization.

D. Comparative Analysis: Effect of SOC on the E-Derived Exciton Doublet

The inclusion of spin–orbit coupling (SOC) modifies both the energetic ordering and optical character of the low-energy excitonic states, as summarized in Table II. In particular, SOC shifts the lowest strongly bright exciton downward by 44.8 meV, from 1.7468 to 1.7020 eV, while changing the quasiparticle gap by only 1 meV. This disparity indicates that the excitonic redshift arises predominantly from changes in the electron–hole interaction rather than from a substantial modification of the quasiparticle band edges. Concurrently, the oscillator strength of the lowest individual bright state decreases by approximately 70.6%. Rather than indicating a loss of optical activity, this reduction reflects a redistribution of optical spectral weight among SOC-mixed excitonic states. The resulting triplet admixture further demonstrates that SOC relaxes the spin-selection constraints of the scalar-relativistic description, allowing nominally spin-forbidden configurations to acquire finite optical intensity.

Figure 8 compares the excitonic band structures and momentum-space distributions of the lowest bright exciton doublet without and with spin–orbit coupling (SOC). Figure 8(a) represents the two no-SOC components β_1 and β_2 together. These states are the nearly degenerate partner functions of the same two-dimensional E irreducible representation of the C_{3v} point group and therefore possess the same excitonic band structure along the Γ–M–K–Γ path. The small numerical splitting of 0.04 meV between β_1 and β_2 does not produce a resolvable difference in their quasiparticle dispersions or in their band-edge electronic character.

Similarly, Fig. 8(b) represents the SOC-renormalized

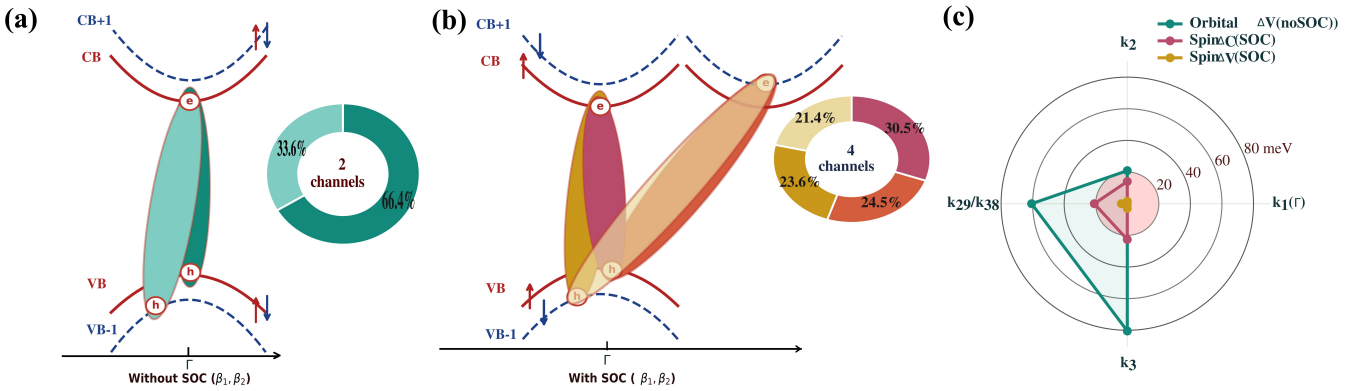


FIG. 7. Microscopic origin of the ground bright bound exciton in monolayer GeSO. (a) Without SOC, the bright doublet β_1, β_2 is formed from the VB→CB and VB−1 →CB transitions, contributing 66.4% and 33.6%, respectively. (b) With SOC, the SOC-renormalized bright doublet is formed from four comparable spinor channels: VB→CB, VB−1 →CB, VB→CB+1, and VB−1 →CB+1, with weights between 21.4% and 30.5%. (c) Momentum-dependent orbital splitting without SOC and SOC-induced splittings of the valence and conduction manifolds; all splittings vanish at Γ.

TABLE II. Comparison of the ground bright doublet without and with SOC.

Quantity	No SOC	SOC	Change
E_X (eV)	1.7468	1.7020	−44.8 meV
E_b (meV)	319.2	363.0	+43.8 meV
S	0.683	0.201	−70.6%
Dominant channels	2	4	+2
Largest share	66.4%	30.5%	−35.9 pp
Spin character	–	24.7% S / 75.3% T	Mixing

bright doublet β_1^{SOC} and β_2^{SOC} together. These two SOC partners occur at 1.70200 and 1.70223 eV, respectively, and are separated by only 0.23 meV. Their nearly identical excitonic band structures demonstrate that SOC preserves the doublet character of the lowest bright excitonic manifold, while redshifting the excitation energy and modifying the spinor composition. Thus, the relevant distinction between Figs. 8(a) and 8(b) is not between the two components within a given doublet, but between the scalar-relativistic and SOC-renormalized descriptions of the same lowest bright exciton manifold.

The corresponding momentum-space distributions are displayed in Figs. 8(c) and 8(d). Within the BSE formalism, the exciton wavefunction is written as a coherent superposition of valence-to-conduction transitions,

$$|\Psi_S\rangle = \sum_{v,c,\mathbf{k}} A^S_{vc\mathbf{k}} \, |v\mathbf{k}; c\mathbf{k}\rangle \, , \tag{24}$$

where $A^S_{vc\mathbf{k}}$ is the excitonic amplitude for a transition from valence band v to conduction band c at crystal momentum $\mathbf{k}$. The momentum-resolved excitonic weight is defined by

$$W^S(\mathbf{k}) = \sum_{v,c} \left| A^S_{vc\mathbf{k}} \right|^2 , \tag{25}$$

which measures the contribution of each crystal momentum to the excitonic state.

Figure 8(c) shows the momentum-space distribution common to the no-SOC doublet β_1, β_2, whereas Fig. 8(d) shows the corresponding distribution for the SOC-renormalized doublet $\beta_1^{\mathrm{SOC}}, \beta_2^{\mathrm{SOC}}$. In both cases, the excitonic weight is strongly localized around the Γ point, with only weak intensity extending toward the K and K′ regions of the first Brillouin zone. This concentration confirms that the lowest bright exciton is primarily a Γ-centered, momentum-direct excitation.

The close similarity between the distributions in Figs. 8(c) and 8(d) shows that SOC does not alter the fundamental momentum-direct nature of the lowest bright exciton. Instead, SOC primarily modifies the internal spinor composition of the electron–hole pair. Without SOC, the β_1, β_2 doublet is formed from two dominant channels, VB→CB and VB−1 →CB. With SOC, the corresponding $\beta_1^{\mathrm{SOC}}, \beta_2^{\mathrm{SOC}}$ doublet becomes a coherent four-channel superposition involving VB→CB, VB−1 →CB, VB→CB+1, and VB−1 →CB+1 transitions. Therefore, SOC redistributes the electron–hole amplitude among spinor band-edge channels while preserving the Γ-centered momentum-space localization of the bright exciton.

At the Γ point, the no-SOC states β_1 and β_2 form the two partner functions of the two-dimensional E irreducible representation of the C_{3v} point group. Their degeneracy is thus symmetry protected. Upon inclusion of SOC, the corresponding states β_1^{SOC} and β_2^{SOC} retain the near-degenerate doublet character, although their excitation energies, oscillator strengths, and spin composition are renormalized. In particular, the SOC doublet contains approximately 24.7% singlet and 75.3% triplet character, demonstrating substantial singlet–triplet mixing. Thus, panels (a) and (c) describe the scalar-relativistic bright doublet, whereas panels (b) and (d) describe its SOC-renormalized counterpart.

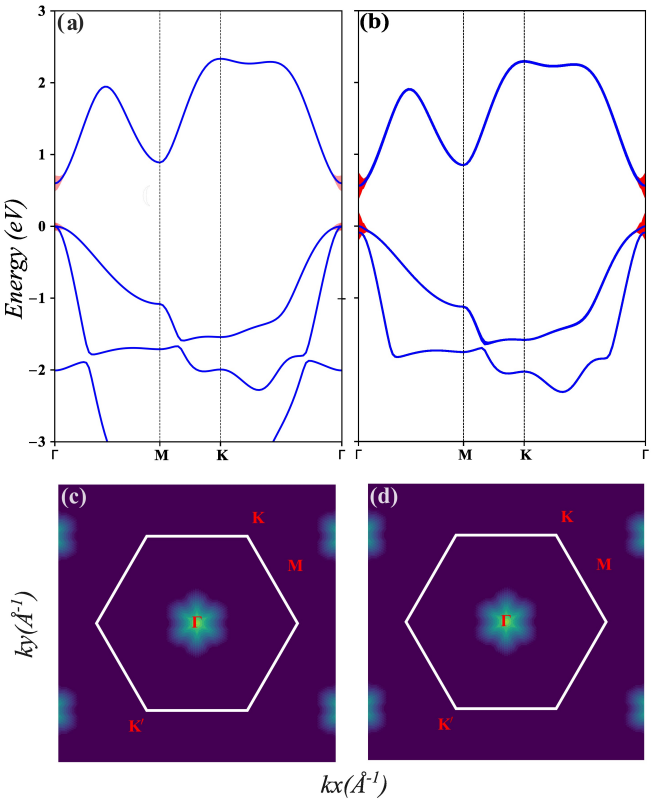


FIG. 8. Excitonic band structures and momentum-space distributions of the lowest bright exciton doublets in monolayer Janus GeSO. (a) Excitonic band structures associated with the nearly degenerate no-SOC bright partners β_1 and β_2 along the high-symmetry path Γ–M–K–Γ. Because β_1 and β_2 are the two symmetry-related components of the same E-derived excitonic doublet, they exhibit essentially identical excitonic band structures. (b) Corresponding excitonic band structures for the SOC-renormalized bright doublet β_1^{SOC} and β_2^{SOC}. (c) Momentum-space excitonic weight, $W^S(\mathbf{k}) = \sum_{v,c} |A^S_{vc\mathbf{k}}|^2$, for the no-SOC doublet β_1, β_2. (d) Corresponding momentum-space distribution for the SOC-renormalized doublet $\beta_1^{\mathrm{SOC}}, \beta_2^{\mathrm{SOC}}$. The weight is strongly concentrated around Γ in both cases, demonstrating that the lowest bright exciton remains predominantly momentum direct after inclusion of SOC.

V. CONCLUSION

We have presented a systematic first-principles study of the electronic and excitonic properties of the Janus GeSO monolayer using G_0W_0 quasiparticle corrections and the Bethe–Salpeter equation. The optimized structure is dynamically stable, with no imaginary phonon modes, and is energetically favorable relative to the elemental constituents and the identified GeS_2–GeO_2 decomposition pathway. These results establish GeSO as a structurally viable two-dimensional platform for exploring many-body optical phenomena.

The quasiparticle calculations show that GeSO is a direct-gap semiconductor with both the VBM and CBM at Γ. The gap increases from 0.60 eV at the PBE level to 2.066 eV within G_0W_0 without SOC, demonstrating that quasiparticle self-energy effects are indispensable for describing this weakly screened monolayer. SOC modifies the gap by only approximately 1 meV, but its influence on the excitonic sector is much stronger. This contrast shows that a nearly unchanged single-particle gap does not imply a negligible SOC effect on optical excitations.

The central result is the identification of the lowest bright exciton as a doubly degenerate E-symmetry state of the C_{3v} point group. Without SOC, the doublet occurs at 1.7468 eV and has a substantial binding energy of 319.2 meV, confirming strong electron–hole attraction in GeSO. The nearby bound state β_0 is nearly dark and transforms as A_2, because this representation is not compatible with the in-plane electric-dipole operator. Thus, the bright–dark ordering and the associated optical selection rules are not accidental features of the calculated spectrum; they follow from the reduced symmetry of the Janus layer.

Including SOC preserves the nearly degenerate bright-doublet structure but changes its microscopic character. The lowest bright states redshift to approximately 1.702 eV and acquire a larger binding energy of about 363 meV. At the same time, the excitonic amplitude changes from a predominantly two-channel orbital superposition to a four-channel spinor superposition, with approximately 24.7% singlet and 75.3% triplet character. The reduced oscillator strength of an individual state should therefore be interpreted as a redistribution of optical weight among SOC-mixed excitonic configurations, rather than as a loss of light–matter coupling. The momentum-space amplitude remains concentrated around Γ, confirming the predominantly Γ-centered character of the lowest exciton. Taken together, our results demonstrate that Janus GeSO combines a direct quasiparticle gap, strong and spectrally distinct excitons, symmetry-protected bright degeneracy, and SOC-controllable spinor mixing. The material therefore offers a promising route toward excitonic devices in which optical activity, polarization response, and spin character can be tuned through symmetry and relativistic interactions. More broadly, the present analysis provides a transferable strategy for separating crystal-symmetry selection rules from SOC- and screening-driven fine structure in Janus and other low-dimensional semiconductors.

AUTHOR CONTRIBUTIONS

Zeeshan Abbas carried out the first-principles calculations, and prepared the initial manuscript draft. Haiying Song conceived and supervised the study, and organized the manuscript. Wenlong Zhang and Haozhe Wang contributed to the data analysis. Danmin Liu contributed to the discussion of the excitonic physics. Shibing Liu contributed to the theoretical interpretation and scientific discussion. All the authors discussed the results,

contributed to the final version of the manuscript, and approved its submission.

DATA AVAILABILITY

All results supporting the findings of this study are presented in the main text. The underlying raw data, including the density functional theory (DFT), G_0W_0, and Bethe–Salpeter equation (BSE) input and output files, with and without spin–orbit coupling (SOC), are available from the authors upon reasonable request.

ACKNOWLEDGEMENTS

The authors sincerely acknowledge the financial support provided by the National Natural Science Foundation of China (No.51875006)

COMPETING INTERESTS

The authors declare no competing interests.

[1] K. S. Novoselov, A. K. Geim, S. V. Morozov, D. Jiang, Y. Zhang, S. V. Dubonos, I. V. Grigorieva, and A. A. Firsov, Science **306**, 666 (2004).

[2] G. Liu, S. B. Liu, B. Xu, C. Y. Ouyang, H. Y. Song, S. Guan, and S. A. Yang, The Journal of Physical Chemistry Letters **6**, 4936 (2015).

[3] Q. H. Wang, K. Kalantar-Zadeh, A. Kis, J. N. Coleman, and M. S. Strano, Nature Nanotechnol. **7**, 699 (2012).

[4] K. F. Mak, C. Lee, J. Hone, J. Shan, and T. F. Heinz, Phys. Rev. Lett. **105**, 136805 (2010).

[5] A. Splendiani, L. Sun, Y. Zhang, T. Li, J. Kim, C.-Y. Chim, G. Galli, and F. Wang, Nano Lett. **10**, 1271 (2010).

[6] C. Ge, Y. Li, H. Song, Q. Xie, L. Zhang, X. Ma, J. Liu, X. Guo, Y. Yan, D. Liu, W. Zhang, S. Liu, and Y. Liu, Nature Communications **15**, 914 (2024).

[7] A. Chernikov, T. C. Berkelbach, H. M. Hill, A. Rigosi, Y. Li, Ö. B. Aslan, D. R. Reichman, M. S. Hybertsen, and T. F. Heinz, Phys. Rev. Lett. **113**, 076802 (2014).

[8] G. Wang, A. Chernikov, M. M. Glazov, T. F. Heinz, X. Marie, T. Amand, and B. Urbaszek, Rev. Mod. Phys. **90**, 021001 (2018).

[9] G. Onida, L. Reining, and A. Rubio, Rev. Mod. Phys. **74**, 601 (2002).

[10] D. Y. Qiu, F. H. da Jornada, and S. G. Louie, Phys. Rev. Lett. **111**, 216805 (2013).

[11] M. F. C. Quintela and N. M. R. Peres, Phys. Status Solidi B **259**, 2200097 (2022).

[12] A.-Y. Lu, H. Zhu, J. Xiao, C.-P. Chuu, Y. Han, M.-H. Chiu, C.-C. Cheng, C.-W. Yang, K.-H. Wei, Y. Yang, Y. Wang, D. Sokaras, D. Nordlund, P. Yang, D. A. Muller, M.-Y. Chou, X. Zhang, and L.-J. Li, Nature Nanotechnol. **12**, 744 (2017).

[13] J. Zhang, S. Jia, I. Kholmanov, L. Dong, D. Er, W. Chen, H. Guo, Z. Jin, V. B. Shenoy, L. Shi, and J. Lou, ACS Nano **11**, 8192 (2017).

[14] L. Dong, J. Lou, and V. B. Shenoy, ACS Nano **11**, 8242 (2017).

[15] A. F. Barbosa, V. N. Freire, and E. W. S. Caetano, Phys. Rev. Mater. **7**, 014001 (2023).

[16] M. S. G. Feuer, A. R.-P. Montblanch, M. Y. Sayyad, C. M. Purser, Y. Qin, E. M. Alexeev, A. R. Cadore, B. L. T. Rosa, J. Kerfoot, E. Mostaani, R. Kałęba, P. Kolari, J. Kopaczek, K. Watanabe, T. Taniguchi, A. C. Ferrari, D. M. Kara, S. Tongay, and M. Atatüre, ACS Nano **17**, 7326 (2023).

[17] S.-H. Lin, J.-M. Zhu, and H.-J. Liu, Phys. Rev. B **111**, 195432 (2025).

[18] C. Liu, T. Liang, X. Sui, L. Du, Q. Guo, G. Xue, C. Huang, Y. You, G. Yao, M. Zhao, J. Yin, Z. Sun, H. Hong, E. Wang, and K. Liu, Nature Commun. **16**, 544 (2025).

[19] R. Peng, Y. Ma, B. Huang, and Y. Dai, Phys. Status Solidi B **259**, 2100562 (2022).

[20] C. Long, Y. Dai, and H. Jin, Phys. Rev. B **104**, 125306 (2021).

[21] A. C. Riis-Jensen, T. Deilmann, T. Olsen, and K. S. Thygesen, ACS Nano **13**, 13354 (2019).

[22] W. Zhou, J. Chen, Z. Yang, J. Liu, and F. Ouyang, Phys. Rev. B **99**, 075160 (2019).

[23] B. Hu, T.-X. Qian, J. Zhou, Y. Ding, T. Cai, and S. Ju, ACS Omega **10**, 30924 (2025).

[24] A. Lukmantoro and M. A. U. Absor, Phys. Rev. Mater. **7**, 104005 (2023).

[25] W.-H. Li, J.-D. Lin, P.-Y. Lo, G.-H. Peng, C.-Y. Hei, S.-Y. Chen, and S.-J. Cheng, Nanomaterials **13**, 1739 (2023).

[26] T. P. T. Linh, N. N. Hieu, H. V. Phuc, C. Q. Nguyen, P. T. Vinh, N. Q. Thai, and N. V. Hieu, RSC Adv. **11**, 39672 (2021).

[27] M. R. Ebrahimi, A. Banjafar, and T. Vazifehshenas, Physica B: Condens. Matter **683**, 415891 (2024).

[28] J. O. D. Godinez, H. N. F. Escamilla, J. de J. Quijano Briones, J. I. P. Ornelas, E. P. Tijerina, R. Ponce-Pérez, D. M. Hoat, and J. G. Sánchez, RSC Adv. **14**, 29160 (2024).

[29] N. T. Tien, R. Ponce-Pérez, A. Reyes-Serrato, J. Guerrero-Sanchez, and D. M. Hoat, Nanoscale Adv. **7**, 7171 (2025).

[30] A. Bakhtatou, I. Ziaya, and K. Zanat, Phys. Scr. **100**, 125965 (2025).

[31] M. B. P. Querne, A. C. Dias, A. Janotti, J. L. F. D. Silva, and M. P. Lima, J. Phys. Chem. C **128**, 12164 (2024).

[32] L. Xiao, G.-C. Guo, H. Luo, M. Zhang, M. You, S. Luo, and J. Zhong, Appl. Surf. Sci. **700**, 163221 (2025).

[33] G. Wang, A. Chernikov, M. M. Glazov, T. F. Heinz, X. Marie, T. Amand, and B. Urbaszek, Rev. Mod. Phys. **90**, 021001 (2018).

[34] E. C. Regan, D. Wang, E. Y. Paik, Y. Zeng, L. Zhang, J. Zhu, A. H. MacDonald, H. Deng, and F. Wang, Nat. Rev. Mater. **7**, 778 (2022).

[35] M. Marsili, A. Molina-Sánchez, M. Palummo, D. Sangalli, and A. Marini, Phys. Rev. B **103**, 155152 (2021).

[36] S. Wang, B. Hu, T.-X. Qian, J. Zhou, Y. Ding, T. Cai, and S. Ju, ACS Appl. Opt. Mater. **3**, 102 (2025).

[37] J. Chen, K. Wu, W. Hu, and J. Yang, J. Phys. Chem. Lett. **12**, 12256 (2021).

[38] S. Gusarov, C. E. Ekuma, G. S. Chang, M. Alizade, and M. Naseri, Phys. Chem. Chem. Phys. **27**, 8158 (2025).

[39] A. Bordoloi, A. C. García-Castro, Z. Romestan, A. H. Romero, and S. Singh, J. Appl. Phys. **135**, 220901 (2024).

[40] P. Giannozzi, S. Baroni, N. Bonini, M. Calandra, R. Car, C. Cavazzoni, D. Ceresoli, G. L. Chiarotti, M. Cococcioni, I. Dabo, A. Dal Corso, S. de Gironcoli, S. Fabris, G. Fratesi, R. Gebauer, U. Gerstmann, C. Gougoussis, A. Kokalj, M. Lazzeri, L. Martin-Samos, N. Marzari, F. Mauri, R. Mazzarello, S. Paolini, A. Pasquarello, L. Paulatto, C. Sbraccia, S. Scandolo, G. Sclauzero, A. P. Seitsonen, A. Smogunov, P. Umari, and R. M. Wentzcovitch, Journal of Physics: Condensed Matter **21**, 395502 (2009).

[41] P. Giannozzi, O. Andreussi, T. Brumme, O. Bunau, M. B. Nardelli, M. Calandra, R. Car, C. Cavazzoni, D. Ceresoli, M. Cococcioni, N. Colonna, I. Carnimeo, A. Dal Corso, S. de Gironcoli, P. Delugas, R. A. Di Stasio, A. Ferretti, A. Floris, G. Fratesi, G. Fugallo, R. Gebauer, U. Gerstmann, P. Giannozzi, J. Jia, M. Kawamura, A. Kokalj, E. Kucukbenli, M. Lazzeri, M. Marsili, N. Marzari, F. Mauri, N. L. Nguyen, H.-V. Nguyen, A. Otero-de-la Roza, L. Paulatto, S. Ponce, D. Rocca, R. Sabatini, B. Santra, M. Schlipf, A. P. Seitsonen, A. Smogunov, I. Timrov, T. Thonhauser, P. Umari, N. Vast, X. Wu, and S. Baroni, Journal of Physics: Condensed Matter **29**, 465901 (2017).

[42] D. Sangalli, A. Ferretti, H. Miranda, C. Attaccalite, I. Marri, E. Cannuccia, P. Melo, M. Marsili, F. Paleari, A. Marrazzo, G. Prandini, P. Bonfà, M. O. Atambo, F. Affinito, M. Palummo, A. Molina-Sanchez, C. Hogan, M. Gruning, D. Varsano, and A. Marini, Journal of Physics: Condensed Matter **31**, 325902 (2019).

[43] D. R. Hamann, Physical Review B **88**, 085117 (2013).

[44] J. P. Perdew, K. Burke, and M. Ernzerhof, Physical Review Letters **77**, 3865 (1996).

[45] H. J. Monkhorst and J. D. Pack, Physical Review B **13**, 5188 (1976).

[46] C. A. Rozzi, D. Varsano, A. Marini, E. K. U. Gross, and A. Rubio, Physical Review B **73**, 205119 (2006).

[47] T. Sohier, M. Calandra, and F. Mauri, Physical Review B **96**, 075448 (2017).

[48] L. Hedin, Physical Review **139**, A796 (1965).

[49] M. S. Hybertsen and S. G. Louie, Physical Review B **34**, 5390 (1986).

[50] G. Onida, L. Reining, and A. Rubio, Reviews of Modern Physics **74**, 601 (2002).

[51] F. Bruneval and X. Gonze, Physical Review B **78**, 085125 (2008).

[52] P. Cudazzo, I. V. Tokatly, and A. Rubio, Physical Review B **84**, 085406 (2011).

[53] P. Cudazzo, Physical Review B **111**, 195122 (2025).

[54] G. Strinati, Rivista del Nuovo Cimento **11**, 1 (1988).

[55] M. Rohlfing and S. G. Louie, Physical Review Letters **81**, 2312 (1998).

[56] V. A. Bastos, F. Paleari, E. Luppi, M. Gibertini, and A. Ruini, arXiv preprint arXiv:2603.04294 (2026), arXiv:2603.04294 [cond-mat.mes-hall].

[57] T.-N. Do, N. N. Hieu, N. A. Poklonski, N. T. T. Binh, C. Q. Nguyen, and N. D. Hien, RSC Advances **11**, 28381 (2021).